Contents lists available at ScienceDirect

Applied Catalysis B: Environmental

Construction of novel ternary component photocatalyst $Sr_{0.25}H_{1.5}Ta_2O_6 \cdot H_2O$ coupled with g-C_3N_4 and Ag toward efficient visible light photocatalytic activity for environmental remediation

Xin Xin [1], Junyu Lang [1], Tingting Wang, Yiguo Su *, Yanxia Zhao, Xiaojing Wang *

College of Chemistry and Chemical Engineering, Inner Mongolia University, Hohhot, Inner Mongolia 010021, PR China

A B S T R A C T

This work reports on the fabrication of a novel ternary component Ag–$Sr_{0.25}H_{1.5}Ta_2O_6 \cdot H_2O$/g-$C_3N_4$ photocatalytic system with highly enhanced visible light photocatalytic activity toward Cr(VI) photoreduction and methyl orange degradation. The result indicated that $Sr_{0.25}H_{1.5}Ta_2O_6 \cdot H_2O$ nanoparticles were deposited on the surface of g-C_3N_4 with high dispersion and that obtained $Sr_{0.25}H_{1.5}Ta_2O_6 \cdot H_2O$/g-$C_3N_4$ heterojunction photocatalyst showed strong absorption in the visible light region. The $Sr_{0.25}H_{1.5}Ta_2O_6 \cdot H_2O$/50 wt%–g-$C_3N_4$ composite displayed increased photocatalytic activity for Cr(VI) photoreduction and methyl orange degradation in comparison with the pristine $Sr_{0.25}H_{1.5}Ta_2O_6 \cdot H_2O$ and g-C_3N_4 under visible light irradiation. The matching of the band structure between $Sr_{0.25}H_{1.5}Ta_2O_6 \cdot H_2O$ and g-C_3N_4 induced an efficient photogenerated electron transfer from the conduction band of g-C_3N_4 to the conduction band of $Sr_{0.25}H_{1.5}Ta_2O_6 \cdot H_2O$, resulting in efficient separation of the photogenerated electron–hole pairs and the subsequent promotion of photocatalytic activity. Moreover, Ag decorated on $Sr_{0.25}H_{1.5}Ta_2O_6 \cdot H_2O$/g-$C_3N_4$ can enhance the visible light absorption efficiency and robustly improve the photocatalytic activity by a factor of 4.7 for Cr(VI) photoreduction and 14.2 for methyl orange degradation, respectively. Ag nanoparticles on $Sr_{0.25}H_{1.5}Ta_2O_6 \cdot H_2O$/g-$C_3N_4$ not only extended the visible light absorption region due to surface plasmon resonance effects, but also acted as an electron mediator as well as an electron acceptor for efficient charge separation.

© 2015 Elsevier B.V. All rights reserved.

1. Introduction

Heterogeneous photocatalysis based on semiconductors utilizing solar energy has been regarded as an effective and green strategy for environmental protection and energy saving, especially for the removal of hazardous organic dyes and heavy metal ions from wastewater [1–3]. Various semiconductors including oxide, sulfide, and oxynitride have been developed for environmental purification. Among them, nano-sized tantalate-based photocatalysts have been extensively investigated due to their excellent photophysical and photochemical properties [4–7]. However, the limited utilization of solar energy and the low separation efficiency of photogenerated electrons and holes result in low visible light photocatalytic activity. In this regard, the development of tantalate-

based photocatalysts with outstanding visible light photocatalytic activity is still urgent and necessary.

Till now, many attempts have been developed to overcome these shortcomings for developing superior visible light photocatalysts, including metal or non-metal doping [8,9], morphology control [10,11], heterojunction [12,13] and so forth. In particular, construction of a semiconductor heterojunction has garnered great research attention because of its perfect effectiveness in improving the photocatalytic activity. Basically, the heterojunction of nano-sized tantalate with narrow bandgap semiconductors usually exhibits a higher photocatalytic performance in comparison with the single-component photocatalyst [14]. The enhanced photocatalytic performance of these heterojunctions is ascribed to the accelerated charge separation by the internal electric field driving force due to their unique band structures including the band gap and energy levels of the conduction band and the valence band [15].

Herein, tantalate-based multi-component heterojunction was taken as the model photocatalytic system based on the following considerations: (i) $Sr_{0.25}H_{1.5}Ta_2O_6 \cdot H_2O$ is a wide band gap and meta-stable phase semiconductor, showing superior photocatalytic activities toward water splitting and benzene degradation

* Corresponding authors. Fax: +86 471 4992981.
   E-mail addresses: cesyg@imu.edu.cn (Y. Su), wang_xiao_jing@hotmail.com (X. Wang).
   [1] Xin Xin and Junyu Lang are co-first authors; they contributed equally to this work.

under ultraviolet light irradiation [16]. An experimental identification of $Sr_{0.25}H_{1.5}Ta_2O_6 \cdot H_2O$ nanoparticles and its relevant heterojunctions is advantageous for tuning the electronic structures and moreover photophysical and photochemical properties of $Sr_{0.25}H_{1.5}Ta_2O_6 \cdot H_2O$ as well as other isostructural nanoparticles. (ii) Graphitic carbon nitride (g-C_3N_4) is a metal-free polymeric photocatalyst with a narrow band gap of 2.7 eV, exhibiting high photocatalytic activity for organic pollutant degradation under visible light irradiation [17–21]. For a heterojunction system, its photocatalytic activity strongly depends on the electronic structure and photoabsorption ability. Based on previous literatures, the conduction band edge potential of g-C_3N_4 is more negative than that of $Sr_{0.25}H_{1.5}Ta_2O_6 \cdot H_2O$, meanwhile the valence band edge potential of g-C_3N_4 is also more negative than the valence band edge potential of $Sr_{0.25}H_{1.5}Ta_2O_6 \cdot H_2O$ [16,22]. Therefore, it is expected that the matching of the band structure between $Sr_{0.25}H_{1.5}Ta_2O_6 \cdot H_2O$ and g-C_3N_4 predicts efficient separation of the photogenerated electron–hole pairs and the subsequent promotion of photocatalytic activity. (iii) Although a variety of binary heterojunction systems has been developed, there are still some drawbacks, such as the limited region of visible light response and low charge separation efficiency. To address these issues, the development of multi-component heterojunction systems is indispensable, which have two or more visible light responsive components and a more efficient charge transfer system [23,24]. In addition to conventional semiconductors, the surface plasmon resonance effect of a noble metal can boost the photoelectrochemical properties and offer a new opportunity to overcome the limited efficiency of photocatalysts and photovoltaic devices [25]. Noble metals (e.g., Au, Ag) can strongly absorb visible light and transfer solar energy to the semiconductor at the energies above and below the band edge through resonant energy transfer, which induces the charge separation and promotes the photocatalytic activity in visible light region [26,27]. On the other hand, noble metallic nanoparticles may also act as electron traps that can facilitate the charge transfer process between semiconductors and enhance the photocatalytic activity [28]. Having these in mind, with the aim of using solar energy to generate electron–hole pairs for boosting photocatalytic activity, it is desirable to construct a ternary heterojunction photocatalytic system, Ag–$Sr_{0.25}H_{1.5}Ta_2O_6 \cdot H_2O$/g-$C_3N_4$ to show highly efficient photocatalytic activity for environmental remediation.

In this work, we report on the fabrication of ternary component Ag–$Sr_{0.25}H_{1.5}Ta_2O_6 \cdot H_2O$/g-$C_3N_4$ heterojunction system for enhanced visible light photocatalytic properties. The coupling effects of g-C_3N_4 and Ag on $Sr_{0.25}H_{1.5}Ta_2O_6 \cdot H_2O$ nanoparticles were systematically studied in an attempt to investigate the possible reasons for the significantly enhanced photocatalytic activity toward reduction of Cr(VI) to Cr(III) and the degradation of methyl orange.

2. Experimental

2.1. Procedure for the synthesis of the Ag–$Sr_{0.25}H_{1.5}Ta_2O_6 \cdot H_2O$/g-$C_3N_4$ composite photocatalysts

2.1.1. Synthesis of $Sr_{0.25}H_{1.5}Ta_2O_6 \cdot H_2O$

All chemicals were of analytical grade and used as raw materials without further purification. In a typical procedure, Sr-based precursor was firstly prepared by dissolving a stoichiometric amount of $SrCl_2 \cdot 6H_2O$ and NaOH in 100 mL distilled water to form a white suspension. After being aged at room temperature for 2 h, the suspension was filtered and washed several times by water. The obtain Sr-based precursor was vacuum dried at 60 °C for 12 h for future use (Fig. S1). Then, 0.418 g of Sr-based precursor and 0.358 g of $TaCl_5$ were dissolved in a mixed solution containing 50 mL of ethanol and 10 mL of 30% hydrogen peroxide under stir-

ring, and then the resultant mixture was transferred into a 100 mL Teflon-lined stainless-steel autoclave. Then, the autoclave was sealed and heated in a preheated oven at 220 °C for 48 h. After the autoclave was air-cooled to room temperature naturally, the resultant product was collected by centrifugation and washed with deionized water and ethanol thoroughly for several times. Finally, $Sr_{0.25}H_{1.5}Ta_2O_6 \cdot H_2O$ white powder was obtained after the sample was centrifuged and dried at 60 °C for 12 h in air.

2.1.2. Synthesis of g-C_3N_4

The g-C_3N_4 was prepared according to previous literature [29]. Briefly, 10 g of melamine (99%) was placed in a alumina crucible and then loaded into the central region of a horizontal tube furnace. The crucible was heated to 550 °C with a heating rate of 10 °C/min and maintained at 550 °C for 4 h, and then allowed to cool to room temperature naturally. The product was washed three times with distilled water to remove soluble reactants and impurities, and then washed three times with ethanol to remove some organic impurities. After drying in a vacuum at 60 °C for 4 h, the yellow agglomerate obtained and ground into powders for further use.

2.1.3. Synthesis of $Sr_{0.25}H_{1.5}Ta_2O_6 \cdot H_2O$/g-$C_3N_4$ heterojunction photocatalyst

Given amount of g-C_3N_4 was dispersed in a beaker containing 20 mL of methanol. The beaker was placed in an ultrasonic bath for 2 h for completely dispersion of g-C_3N_4. Then, the $Sr_{0.25}H_{1.5}Ta_2O_6 \cdot H_2O$ powder was added into the above suspension and stirred in a fume hood for 24 h. After volatilization of the methanol, the resultant yellow solid was collected and dried in a vacuum oven at 60 °C for 12 h. The weight ratios of g-C_3N_4 to $Sr_{0.25}H_{1.5}Ta_2O_6 \cdot H_2O$ was fixed to be 17 wt%, 33 wt%, 50 wt%, 67 wt%, and 83 wt%.

2.1.4. Synthesis of Ag–$Sr_{0.25}H_{1.5}Ta_2O_6 \cdot H_2O$/g-$C_3N_4$ heterojunction photocatalyst, as shown in Fig. 8

The 0.2 g of $Sr_{0.25}H_{1.5}Ta_2O_6 \cdot H_2O$/g-$C_3N_4$ powder was dispersed in a methyl orange aqueous solution (20 mg/L) in a flask. The solution was constantly stirred using a magnetic stirrer for 1 h at room temperature in dark. Then, the adequate amount of $AgNO_3$ solution (Ag quantities was fixed to 0.5 wt%, 1 wt%, 1.5 wt%, 2 wt%, and 2.5 wt% compared to $Sr_{0.25}H_{1.5}Ta_2O_6 \cdot H_2O$/g-$C_3N_4$ heterojunction photocatalyst) was added to the resulted solution and irradiated using a 300 W Xenon (Xe) lamp with a 420 nm long pass filter in atmosphere with stirring for 2 h. The obtained suspension of particles was collected and dried in a vacuum oven at 60 °C.

2.2. Sample characterization

Wide-angle X-ray power diffraction (XRD) was recorded on a Rigaku DMAX2500 X-ray diffractometer with Cu Kα radiation to identify the phase structures of all samples. Transmission electron microscopy (TEM) was performed on a JEM-2010 apparatus with an acceleration voltage of 200 kV, which used to determine the particle sizes and morphologies of the samples. The samples for the TEM measurements were suspended in ethanol by ultrasonic dispersion and supported on a Cu grid. The optical diffuse reflectance spectra of the samples were characterized on a PerkinElmer UV/VS/NIR Lambda 750s spectrometer using $BaSO_4$ for the corrected baseline. Infrared spectra of the samples were recorded on a PerkinElmer IR spectrometer using a KBr pellet technique. The surface photocurrent measurement was carried out based on a lock-in amplifier [30]. The measurement system is constructed by a sample chamber, a lock-in amplifier (SR 830, Stanford Research Systems, Inc.) with a light chopper (SR540, Stanford Research Systems, Inc.) and a source of monochromatic light which

is provided by a 500 W xenon lamp (CHF-XM 500, Trusttech) and a monochromator (Omni-λ300, Zolix). The monochromator and the lock-in amplifier were equipped with a computer. The analyzed product is assembled as a sandwich-like structure of ITO-product-ITO, which ITO means an indium tin oxide electrode. XPS analyses were carried out on an ESCALab220i-XL with a monochromatic Al Kα and charge neutralizer. The deconvolution software program was provided by Kratos. This software is the standard program used and is accepted as reference in the field. All the binding energies were referenced to the C 1s peak at 284.6 eV. Powder samples were prepared by deposition of catalyst on carbon type stuck to sample holder. The powder samples were analyzed with very large spot of a dimension 0.3×0.7 mm. ESR spectra were performed by an ER200-SRC electron spin resonance spectrometer (Bruker, Germany) at 3186 G and 9056.895 MHz. ESR spectra for hydroxyl radicals (aqueous solution volume, 2.0 mL; sample, 4 mg; DMPO, 0.22 M.) in dark and under visible light irradiation. ESR spectra for superoxide radicals (methanol solution volume, 2.0 mL; sample, 4 mg; DMPO, 0.22 M.) in dark and under visible light irradiation. Emission spectra and transient decays of the samples were recorded on an Edinburgh Instruments FLS920 spectrofluorimeter equipped with both continuous and pulsed xenon lamps. Detection of the signals was achieved with a photomultiplier tube (PMT) (R955, Hamamatsu) in the UV and visible regions. Lifetime measurement was performed with the same spectrophotometer and detectors using a Plused Hydrogen lamp (nF900, Edinburgh) with a pulse width of about 1.6 ns. The signals were detected with a photomultiplier tube (PMT) (R955, Hamamatsu) in the UV and visible regions. The resolution of both excitation and emission spectra is maintained at about 1 nm for all runs. All spectra recorded were ratio corrected to remove the wavelength dependent intensity of the lamp. The wavelength of excitation light for emission spectra and transient decays was 328 nm for all samples. The Chromatographic experiments with HPLC–UV/vis system were carried out to monitor the degradation process of methyl orange. The total organic carbon (TOC) data was measured using a Elementar Vario analyzer.

2.3. Photocatalytic reactivity test

The photocatalytic activities of the as-prepared heterojunction photocatalysts were evaluated by the degradation of methyl orange (MO: 20 mg/L) in H_2O and the Cr(VI) photoreduction. Herein, the procedure of MO aqueous solution degradation experiments was as follows: At first, 25 mg of the as-prepared samples were dispersed in a 100 mL beaker containing 50 mL of the organic substance solution to form homogeneous suspension and were stirred for 2 h to establish the equilibrium of MO absorption–desorption on the sample surfaces before illumination. Then, all suspensions were transferred to a water-cooled reactor and irradiated under a 300 W mercury lamp with a filter ($\lambda \geq 420$ nm). Subsequently, 3 mL of suspension was collected at given time intervals and then filtered with the centrifuge to remove the as-prepared photocatalysts. The supernatants were dropped in a cuvette to record the UV–vis absorption spectra at 464 nm by a UVIKON XL/XS spectrometer.

The Cr(VI) stock solution (10 mg/L) was prepared by dissolving $K_2Cr_2O_7$ in deionized water. Then, 25 mg of powder photocatalyst were dispersed in 50 mL of Cr(VI) solution and stirred in the dark for 2 h at room temperature to establish adsorption–desorption equilibrium. Under stirring, the all mixed suspension was exposed to visible light irradiation produced under a 300 W mercury lamp ($\lambda \geq 420$ nm). At given time intervals, 3 mL of suspension was extracted and centrifuged to separate the as-prepared photocatalyst. The color of the solution was developed via the diphenylcarbazide (DPC) method according to previous literature [31]. The concentration of Cr(VI) was determined by measuring
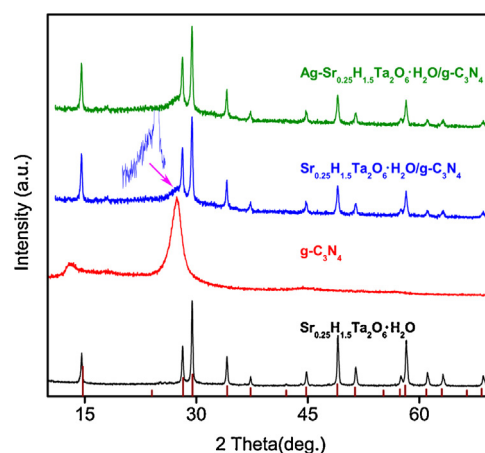

Fig. 1. XRD patterns of the as-prepared photocatalysts. Vertical bars represents the standard data of $Sr_{0.25}H_{1.5}Ta_2O_6 \cdot H_2O$ (JCPDS Card No. 77-1170).

its absorption wavelength of 540 nm using a UVIKON XL/XS spectrophotometer.

3. Results and discussion

$Sr_{0.25}H_{1.5}Ta_2O_6 \cdot H_2O$ is a meta-stable phase semiconductor that was often obtained by traditional solid state and proton-exchange approaches. Although the synthesis of $Sr_{0.25}H_{1.5}Ta_2O_6 \cdot H_2O$ can be achieved by a hydrothermal method, hydrofluoric acid was used as the raw material, which is extremely corrosive and a contact poison. This work reported a environmental benign hydrothermal method by using Sr-based precursor and $TaCl_5$ as raw materials. The XRD pattern of the as-prepared $Sr_{0.25}H_{1.5}Ta_2O_6 \cdot H_2O$ is shown in Fig. 1. It is found that all diffraction peaks could be well-indexed to a pure cubic phase of $Sr_{0.25}H_{1.5}Ta_2O_6 \cdot H_2O$ (Joint Committee on Powder Diffraction Standards (JCPDS) card no. 77-1170), which is similar to Wu's results [16]. By the least-squares method using the Retica Rietveld program, the lattice parameter was determined to be $a = 10.481$ Å, which is slightly smaller than the standard value of $Sr_{0.25}H_{1.5}Ta_2O_6 \cdot H_2O$. The narrowed diffraction peaks indicated the fine nature and high crystallinity of $Sr_{0.25}H_{1.5}Ta_2O_6 \cdot H_2O$. The peak broadening was used to calculated the crystalline size of the primary particles. On the basis of the half-height width of the (1 1 1) peak, the mean particle size for $Sr_{0.25}H_{1.5}Ta_2O_6 \cdot H_2O$ was calculated to be around 39.4 nm. Besides $Sr_{0.25}H_{1.5}Ta_2O_6 \cdot H_2O$, the XRD pattern of g-$C_3N_4$ is also given in Fig. 1. From Fig. 1, it is seen that two peaks were observed for the as-prepared g-C_3N_4 sample. The strongest peak at $2\theta = 27.29°$ is a characteristic interlayer stacking peak of aromatic systems, which is indexed as the (0 0 2) peak for graphitic carbon nitride. The small angle peak at $2\theta = 12.99°$ corresponds to the interplanar distance, which is indexed to be (1 0 0) peak [32]. The main characteristic diffraction peaks of $Sr_{0.25}H_{1.5}Ta_2O_6 \cdot H_2O$/g-$C_3N_4$ did not obviously change after $Sr_{0.25}H_{1.5}Ta_2O_6 \cdot H_2O$ coupled with g-C_3N_4. No apparent diffraction peaks belonging to g-C_3N_4 was observed for $Sr_{0.25}H_{1.5}Ta_2O_6 \cdot H_2O$/g-$C_3N_4$ (weight ratio of g-C_3N_4 to $Sr_{0.25}H_{1.5}Ta_2O_6 \cdot H_2O < 33$ wt%) (Fig. S2). However, with increasing g-C_3N_4 content to 50 wt%, the weak diffraction peak of g-C_3N_4 could be found as illustrated in inset of Fig. 1, which is further confirmed by the XRD patterns with more g-C_3N_4 content (Fig. S2). This result confirmed the co-existence of g-C_3N_4 and $Sr_{0.25}H_{1.5}Ta_2O_6 \cdot H_2O$ in $Sr_{0.25}H_{1.5}Ta_2O_6 \cdot H_2O$/g-$C_3N_4$ heterojunctions. Moreover, it is also noted that Ag decorated on $Sr_{0.25}H_{1.5}Ta_2O_6 \cdot H_2O$/g-$C_3N_4$ led to no apparent alteration of the diffraction peaks, which may be related to small particle sizes and low heterojunction content of Ag. The fine
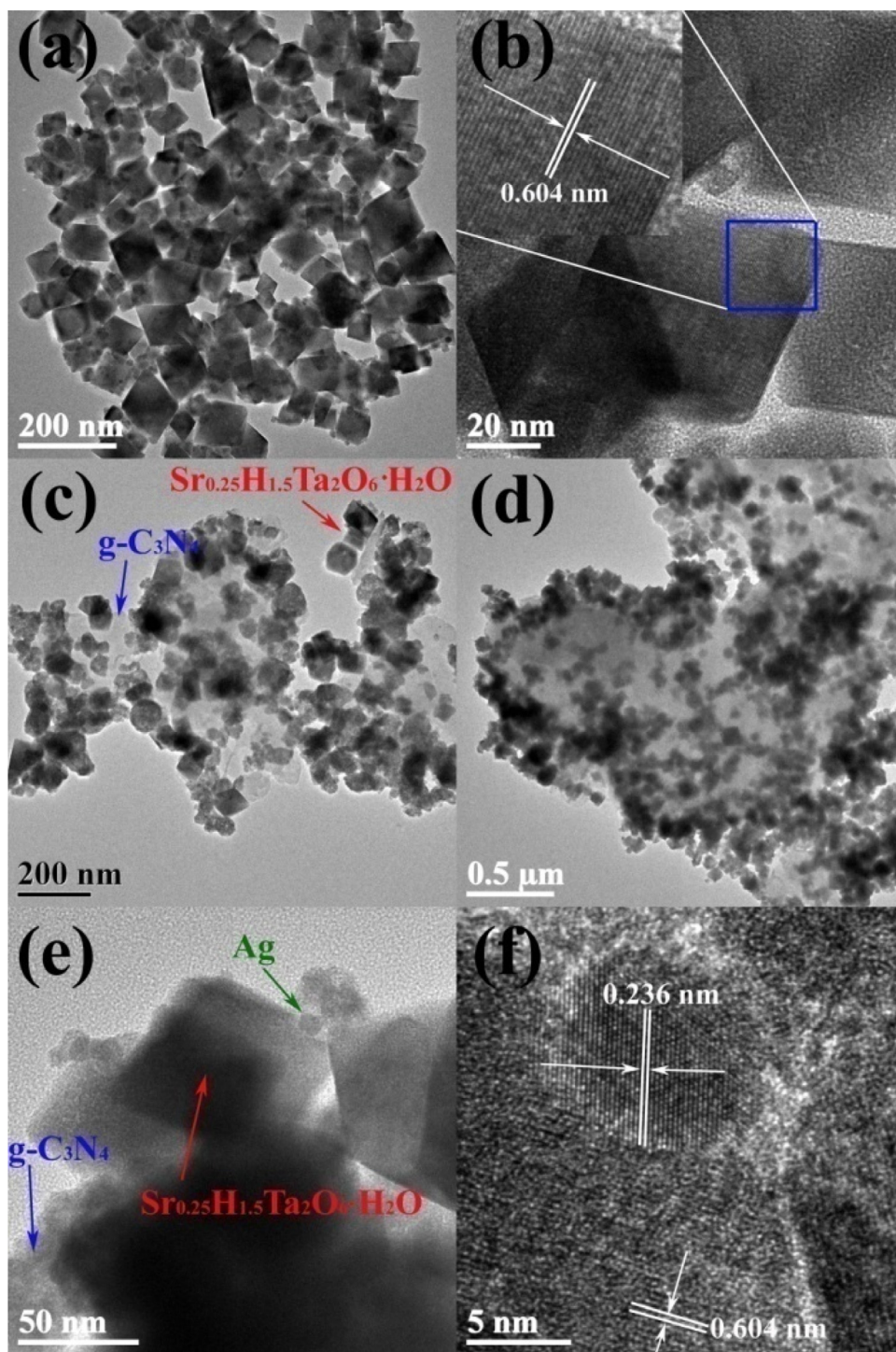
Fig. 2. TEM (a) and HRTEM (b) images of pure $Sr_{0.25}H_{1.5}Ta_2O_6·H_2O$ nanoparticles, TEM (c) image of $Sr_{0.25}H_{1.5}Ta_2O_6·H_2O/g-C_3N_4$ heterojunction, TEM image (d) of Ag–$Sr_{0.25}H_{1.5}Ta_2O_6·H_2O/g-C_3N_4$, high-magnification TEM image (e) and HRTEM images of Ag–$Sr_{0.25}H_{1.5}Ta_2O_6·H_2O/g-C_3N_4$.

nature and heterojunction feature of Ag–$Sr_{0.25}H_{1.5}Ta_2O_6·H_2O/g-C_3N_4$ were also confirmed by TEM observations.

The detailed characterization of the morphologies, crystal structures and the heterojunction features of the as-prepared photocatalysts was based on transmission electron microscopy (TEM) and high-resolution TEM (HRTEM). Fig. 2a shows the TEM image of the pristine $Sr_{0.25}H_{1.5}Ta_2O_6·H_2O$ nanoparticles. It can be seen that the morphology of pristine $Sr_{0.25}H_{1.5}Ta_2O_6·H_2O$ is well-crystallized octahedron (Fig. S3) with average diameter of about 50 nm, which is a bit larger than the XRD calculated results. The

HRTEM image in Fig. 2b reveals that distance between the adjacent lattice fringes is about 0.604 nm, being close to 0.609 nm of (1 1 1) plane for $Sr_{0.25}H_{1.5}Ta_2O_6·H_2O$ (JCPDS card no. 77-1170). As for $Sr_{0.25}H_{1.5}Ta_2O_6·H_2O/g-C_3N_4$, two types of materials were found in the 50 wt% $Sr_{0.25}H_{1.5}Ta_2O_6·H_2O/g-C_3N_4$, which corresponded to g-C_3N_4 and $Sr_{0.25}H_{1.5}Ta_2O_6·H_2O$, respectively, as illustrated in Fig. 2c. This observation suggests that g-C_3N_4 served as the support to bind $Sr_{0.25}H_{1.5}Ta_2O_6·H_2O$ nanoparticles in this heterojunction system. The TEM image for the 1.5 wt% Ag modified $Sr_{0.25}H_{1.5}Ta_2O_6·H_2O/g-C_3N_4$ sample shows similar feature with
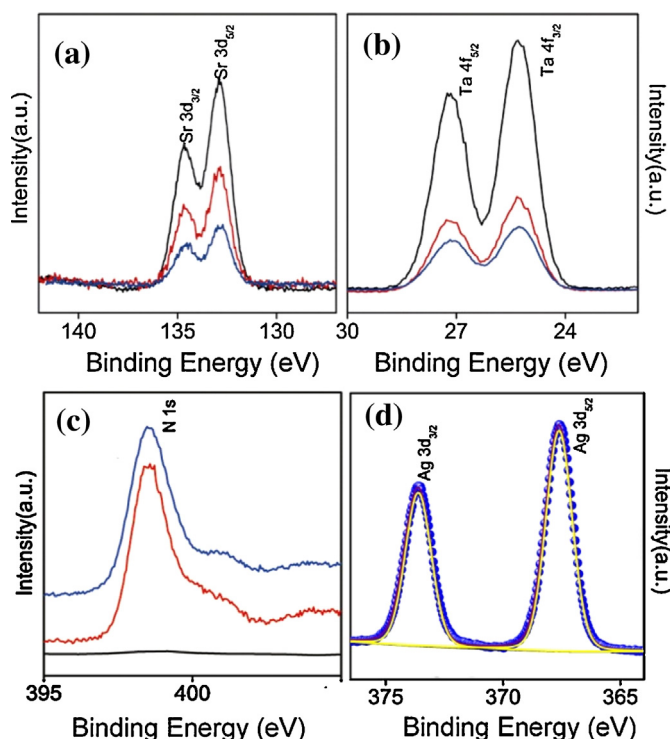
Fig. 3. XPS spectra of the as-prepared photocatalysts. The black, red and blue lines represent $Sr_{0.25}H_{1.5}Ta_2O_6 \cdot H_2O$, $Sr_{0.25}H_{1.5}Ta_2O_6 \cdot H_2O/g\text{-}C_3N_4$, and Ag–$Sr_{0.25}H_{1.5}Ta_2O_6 \cdot H_2O/g\text{-}C_3N_4$, respectively. (For interpretation of the references to color in this figure legend, the reader is referred to the web version of this article.)

that of $Sr_{0.25}H_{1.5}Ta_2O_6 \cdot H_2O/g\text{-}C_3N_4$ heterojunction system, where $Sr_{0.25}H_{1.5}Ta_2O_6 \cdot H_2O$ nanoparticles were deposited on the surface of g-C_3N_4 with high dispersion. No apparent Ag nanoparticles were observed. To further specify the location of Ag nanoparticles, a high-magnified TEM image is shown in Fig. 2e. As shown in Fig. 2e, the co-existence of $Sr_{0.25}H_{1.5}Ta_2O_6 \cdot H_2O$, g-$C_3N_4$, and Ag was observed. The corresponding HRTEM image is illustrated in Fig. 2f. The spacing between adjacent lattice fringes was 0.236 nm, which is close to that of 0.237 nm for the (1 1 1) plane of Ag (JCPDS Card No. 01-1164), indicating the crystalline nature and the presence of Ag nanoparticles in the heterojunction photocatalyst. It is noted that another lattice plane space of 0.604 nm was also observed, which is compatible with 0.609 nm of (1 1 1) plane for $Sr_{0.25}H_{1.5}Ta_2O_6 \cdot H_2O$ (JCPDS card no. 77-1170). Moreover, the EDS data (Fig. S4) confirmed that the main elemental components are N, C, O, Sr, Ta, and Ag, which is also confirmed by scanning transmission electron microscopy (STEM) data (Fig. S5). The signal of Cu from the TEM grid was also detected. The EDS and STEM data are in accordance with that of HRTEM image. From Fig. 2f, it is concluded that a ∼8 nm Ag nanoparticle was grafted on the surface of $Sr_{0.25}H_{1.5}Ta_2O_6 \cdot H_2O$ nanoparticles.

XPS technique was further used to investigate the composition of the as-prepared photocatalysts. Fig. 3a shows the XPS spectra of Sr 3d in $Sr_{0.25}H_{1.5}Ta_2O_6 \cdot H_2O$, $Sr_{0.25}H_{1.5}Ta_2O_6 \cdot H_2O/g\text{-}C_3N_4$, and Ag–$Sr_{0.25}H_{1.5}Ta_2O_6 \cdot H_2O/g\text{-}C_3N_4$, respectively. It is seen that the Sr 3d XPS signal in all samples gave identical binding energies at 134.5 eV and 132.9 eV, which can be ascribed to the typical Sr $3d_{3/2}$ and Sr $3d_{5/2}$, respectively, being in consistent with the reference value [33]. The Ta 4f XPS signal was also observed for all samples. As shown in Fig. 3b, two strong XPS peaks with the binding energies of 25.3 eV and 27.2 eV can be ascribed to the Ta $4f_{7/2}$ and Ta $4f_{5/2}$ of Ta^{5+}, respectively, in good agreement with reference results [34]. As for N 1s XPS signal (Fig. 3c), it is seen that
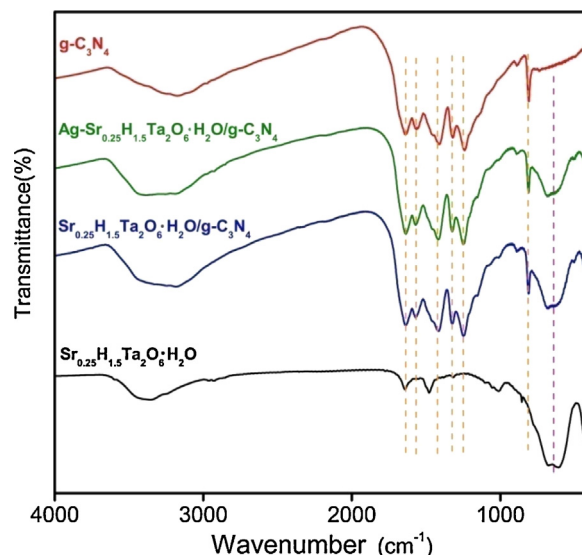
pure $Sr_{0.25}H_{1.5}Ta_2O_6 \cdot H_2O$ gave no apparent N 1s peak. However, for $Sr_{0.25}H_{1.5}Ta_2O_6 \cdot H_2O/g\text{-}C_3N_4$ and Ag–$Sr_{0.25}H_{1.5}Ta_2O_6 \cdot H_2O/g\text{-}C_3N_4$ samples, similar multi-component peak feature was observed. Peak deconvolution on N1s signal for Ag–$Sr_{0.25}H_{1.5}Ta_2O_6 \cdot H_2O/g\text{-}C_3N_4$ (Fig. S6) indicated that four signal components exists in N 1s XPS signal. The strong N 1s signals appeared at 398.4 eV, 399.7 eV, and 400.7 eV, which were assigned to sp2 hybridized aromatic N bonded to carbon atoms (C=N—C) and quaternary N bonded three carbon atoms in the aromatic cycles, respectively [35]. A weak XPS peak at 404.2 eV was also observed, which is attributed to the π-excitations [36], implying that the coupling of $Sr_{0.25}H_{1.5}Ta_2O_6 \cdot H_2O$ cover up to the π-excitations and coupled with g-C_3N_4 via a interaction using π-electrons of CN heterocycles. Moreover, the deconvolution of C 1s XPS signal for Ag–$Sr_{0.25}H_{1.5}Ta_2O_6 \cdot H_2O/g$-$C_3N_4$ (Fig. S6) indicated that at least three C 1s XPS peaks locating at 284.6 eV, 286.2 eV and 287.6 eV were observed, being in accordance with that observed in g-C_3N_4-M^{n+}/CeO$_2$–TiO$_2$ ternary composites [37]. To further shed light on the chemical state of Ag in Ag–$Sr_{0.25}H_{1.5}Ta_2O_6 \cdot H_2O/g\text{-}C_3N_4$ heterojunction photocatalyst, the Ag 3d XPS signal was also investigated. Interestingly, it can be seen that the deconvoluted Ag 3d peaks in Fig. 3d indicated that single component exists in Ag $3d_{5/2}$ and Ag $3d_{3/2}$ signals. According to previous literature [38], the peaks at about 368.1 eV and 374.1 eV should be assigned to metallic silver (Ag^0). No signals belonging to Ag$^+$ was observed. This result implied that Ag nanoparticles were deposited on the surfaces of $Sr_{0.25}H_{1.5}Ta_2O_6 \cdot H_2O/g\text{-}C_3N_4$ heterojunction photocatalyst, which may have significant impact on the photocatalytic activities.

The surface chemistry and the heterojunction feature of the as-prepared photocatalysts were characterized using FT-IR spectroscopy. Fig. 4 shows a comparison of FT-IR spectra of pristine $Sr_{0.25}H_{1.5}Ta_2O_6 \cdot H_2O$, g-$C_3N_4$ and their heterojunctions. It can be seen that all samples gave a broad absorption band at about 3350 cm^{-1}, which is attributed to the typical vibrations of O—H bonds for water adsorbed on sample surfaces [39]. For pristine $Sr_{0.25}H_{1.5}Ta_2O_6 \cdot H_2O$, an intense broad band appeared in the region from 1000 to 480 cm^{-1} is related to the typical Ta—O vibration [40]. Whereas, g-C_3N_4 showed a series of absorption peaks in the region from 1700 to 800 cm^{-1}. The peak at 1643 cm^{-1} is attributed to C=N stretching vibration modes, while the peaks at 1568, 1423, 1320, and 1245 cm^{-1} are related to aromatic C—N stretching vibrations [35]. A sharp absorption peak at 808 cm^{-1} is related to the s-triazine ring modes [41]. The FT-
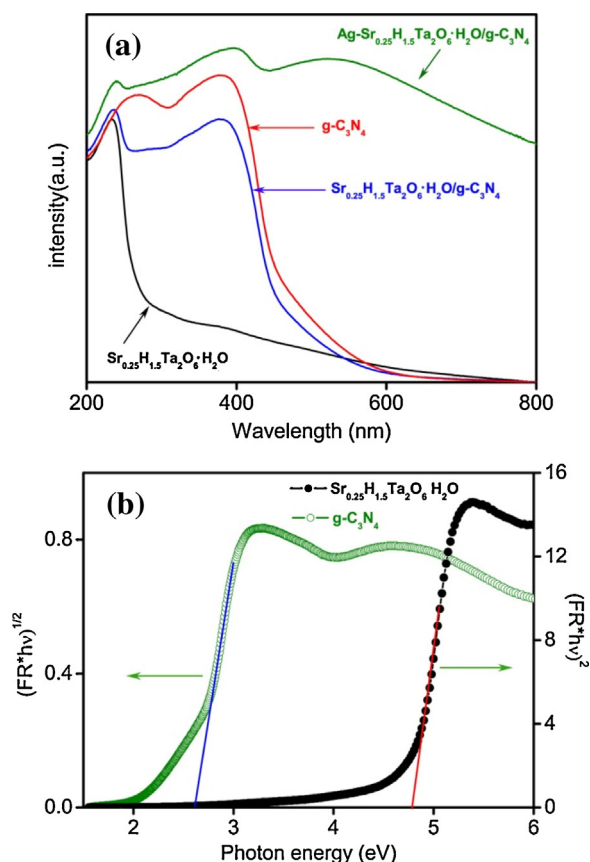

Fig. 4. FT-IR spectra of the as-prepared photocatalysts.

Fig. 5. UV–visible diffuse reflectance spectra of the as-prepared photocatalysts (a) and the optical bandgap of pristine $Sr_{0.25}H_{1.5}Ta_2O_6\cdot H_2O$ and g-C_3N_4 (b).

IR spectra of $Sr_{0.25}H_{1.5}Ta_2O_6\cdot H_2O$/g-$C_3N_4$ (weight ratio of g-C_3N_4 to $Sr_{0.25}H_{1.5}Ta_2O_6\cdot H_2O$ = 50 wt%) and Ag–$Sr_{0.25}H_{1.5}Ta_2O_6\cdot H_2O$/g-$C_3N_4$ (weight ratio of Ag to $Sr_{0.25}H_{1.5}Ta_2O_6\cdot H_2O$/g-$C_3N_4$ = 1.5 wt%) heterojunctions are similar to those of the main peaks of pure g-C_3N_4 and $Sr_{0.25}H_{1.5}Ta_2O_6\cdot H_2O$, suggesting that no structural change of g-C_3N_4 and $Sr_{0.25}H_{1.5}Ta_2O_6\cdot H_2O$ occurred during the heterojunction process. However, it's noted that a minor blue shift of the s-triazine ring vibration occurred after heterojunction of $Sr_{0.25}H_{1.5}Ta_2O_6\cdot H_2O$ nanoparticles on g-C_3N_4 surfaces (Fig S7), implying that there may exist weak covalent interactions between g-C_3N_4 and $Sr_{0.25}H_{1.5}Ta_2O_6\cdot H_2O$ [42].

The bandgap and energy level of the oxide semiconductors play a critical role in modulating their photocatalytic performance. Fig. 5a shows the UV–visible diffuse reflectance spectra of the as-prepared photocatalysts. As illustrated in Fig. 5a, pristine $Sr_{0.25}H_{1.5}Ta_2O_6\cdot H_2O$ showed an intense absorption band in the range of 200–300 nm, which is ascribed to the typical electronic transition from the O 2p to the Ta 5d orbital [16]. While g-C_3N_4 showed absorption edge at around 480 nm, suggesting g-C_3N_4 can absorb solar energy with a wavelength shorter than 480 nm. $Sr_{0.25}H_{1.5}Ta_2O_6\cdot H_2O$/g-$C_3N_4$ (weight ratio of g-C_3N_4 to $Sr_{0.25}H_{1.5}Ta_2O_6\cdot H_2O$ = 50 wt%) exhibited similar absorption feature in comparison with g-C_3N_4, indicating that $Sr_{0.25}H_{1.5}Ta_2O_6\cdot H_2O$/g-$C_3N_4$ heterojunction photocatalyst should possess visible light photocatalytic activity. Interestingly, compared with $Sr_{0.25}H_{1.5}Ta_2O_6\cdot H_2O$, g-$C_3N_4$ and $Sr_{0.25}H_{1.5}Ta_2O_6\cdot H_2O$/g-$C_3N_4$, Ag decorated $Sr_{0.25}H_{1.5}Ta_2O_6\cdot H_2O$/g-$C_3N_4$ photocatalyst exhibited an obviously enhanced visible light absorption extending to 800 nm. The intense and broad absorption larger than 460 nm should originate from the strong surface plasmon resonance of Ag nanoparticles [43]. The optical bandgap near

the band edge (Fig. 5b) of $Sr_{0.25}H_{1.5}Ta_2O_6\cdot H_2O$ and g-C_3N_4 was also determined according to the following equation

$$\alpha h\nu = A\left(h\nu - E_g\right)^{n/2}$$

where α, ν, E_g, A and n are the absorption coefficient, incident light frequency, band gap, constant, and an integer, respectively. The value of n as determined for $Sr_{0.25}H_{1.5}Ta_2O_6\cdot H_2O$ is 1 due to a direct optical transition type for $Sr_{0.25}H_{1.5}Ta_2O_6\cdot H_2O$ [16]. Whereas, the value of n for g-C_3N_4 was determined to be 4 because of an indirect optical transition type [44]. Finally, as shown in Fig. 4b, the optical bandgap of $Sr_{0.25}H_{1.5}Ta_2O_6\cdot H_2O$ and g-C_3N_4 was calculated to be 4.78 eV and 2.62 eV, respectively, which are close to previously reported values [16,17,44].

Since the heterojunction of $Sr_{0.25}H_{1.5}Ta_2O_6\cdot H_2O$ on g-C_3N_4 can result in the absorption of solar energy, it is expected that $Sr_{0.25}H_{1.5}Ta_2O_6\cdot H_2O$/g-$C_3N_4$ may show visible light photocatalytic activity. The photocatalytic activity of $Sr_{0.25}H_{1.5}Ta_2O_6\cdot H_2O$/g-$C_3N_4$ heterojunctions was evaluated using Cr(VI) photoreduction and methyl orange degradation as the model reactions. Fig. 6a shows the time courses of photocatalytic reduction of Cr(VI) to Cr(III) in an aqueous suspension of the as-prepared photocatalysts under visible light irradiation. For comparison, the photocatalytic reduction of Cr(VI) without catalyst was also carried out. The result showed that Cr(VI) is stable under visible light irradiation in the absence of any catalyst (Fig. S8). However, after addition of catalyst into Cr(VI) solution, obviously, the photocatalytic activity of $Sr_{0.25}H_{1.5}Ta_2O_6\cdot H_2O$/g-$C_3N_4$ heterojunctions can be well tuned as a function of g-C_3N_4 weight ratios. Pristine $Sr_{0.25}H_{1.5}Ta_2O_6\cdot H_2O$ nanoparticles exhibited no apparent photocatalytic activity toward the reduction of Cr(VI). However, with an increase of g-C_3N_4 weight ratio from 17 wt% to 50 wt%, $Sr_{0.25}H_{1.5}Ta_2O_6\cdot H_2O$/g-$C_3N_4$ heterojunctions exhibited greatly enhanced photocatalytic activity, while further increase of g-C_3N_4 content led to an obvious decrease of the photocatalytic activity toward Cr(VI) reduction. Similar results have been observed in many g-C_3N_4-based heterojunctions, including ZnWO$_4$/g-C_3N_4, In$_2$S$_3$/g-C_3N_4, BiOBr/g-C_3N_4 and so on [35,41]. The possible reason is that suitable component of $Sr_{0.25}H_{1.5}Ta_2O_6\cdot H_2O$ and g-C_3N_4 could generate more heterojunction interface for efficient separation of photogenerated electron–hole pairs [45], thus leading to optimized photocatalytic activity. Methyl orange degradation via semiconductor photocatalysis has been often used as a model reaction to evaluate the photocatalytic performance of various photocatalysts [46–51]. Fig. 6b shows the concentration changes of methyl orange versus visible light irradiation time. Similar to Cr(VI), methyl orange displayed no obvious self-degradation at the absence of any catalyst (Fig. S9). It can be seen that both pristine $Sr_{0.25}H_{1.5}Ta_2O_6\cdot H_2O$ and g-C_3N_4 showed very weak photocatalytic activity toward the degradation of methyl orange. However, the photocatalytic activity was highly improved after the heterojunction of $Sr_{0.25}H_{1.5}Ta_2O_6\cdot H_2O$ on g-C_3N_4 surfaces, which showed a maximum at g-C_3N_4 weight ratio of 50 wt%. Further comparative studies of the concentration changes of Cr(VI) and methyl orange with visible light irradiation time for $Sr_{0.25}H_{1.5}Ta_2O_6\cdot H_2O$, g-$C_3N_4$ and $Sr_{0.25}H_{1.5}Ta_2O_6\cdot H_2O$/50 wt%-g-$C_3N_4$ are shown in Fig. 6c and d. It is seen that there existed a linear relationship between the ln(C/C_0) plot and visible light irradiation time. This result indicated that the photoreduction of Cr(VI) and degradation of methyl orange followed a pseudo-first-order kinetic feature, which can be described as follows

$$\ln\left(\frac{C}{C_0}\right) = -kt$$

where C is Cr(VI)/methyl orange concentration at time t, C_0 is the initial Cr(VI)/methyl orange concentration, and k
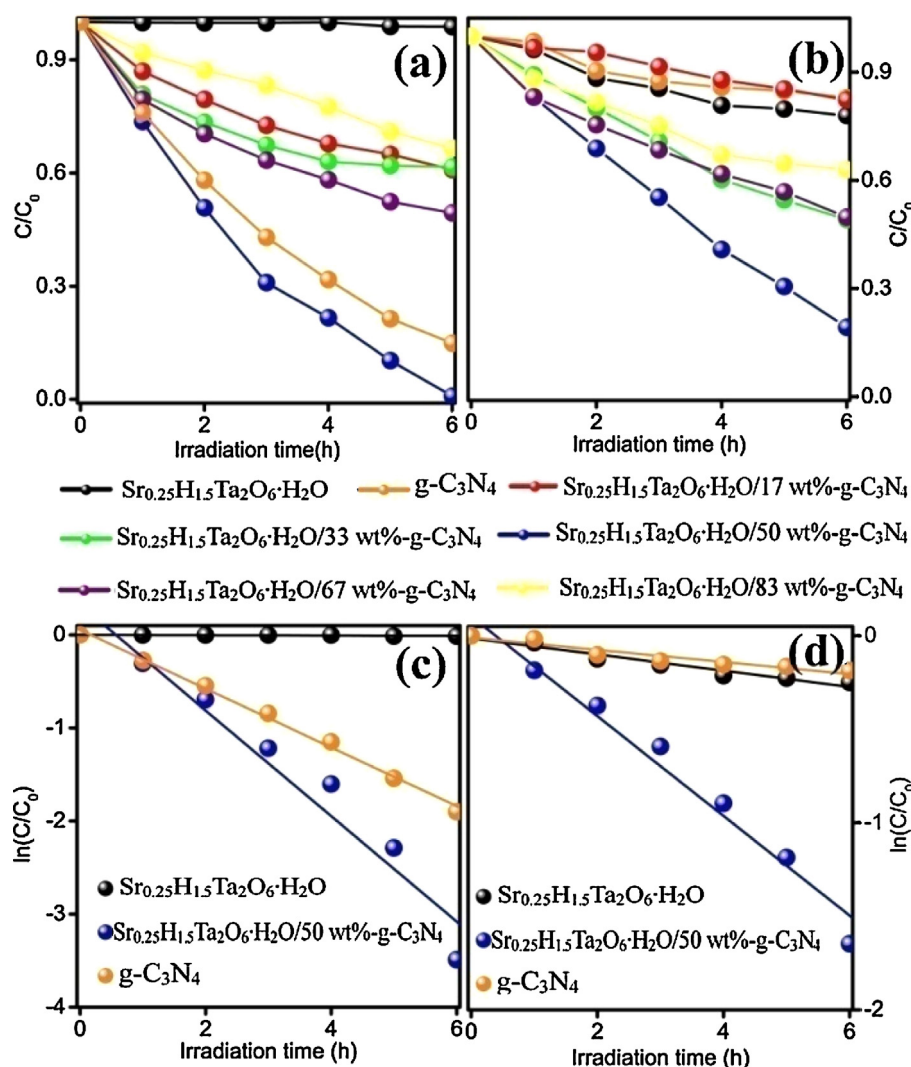
Fig. 6. Normalized concentration of Cr(VI) versus visible light irradiation time in the presence of as-prepared photocatalysts (a), methyl orange concentration changes as a function of visible light irradiation time (b), relationship between $\ln(C/C_0)$ and time for the photoreducition of Cr(VI) (c) and degradation of methyl orange (d) over pristine $Sr_{0.25}H_{1.5}Ta_2O_6\cdot H_2O$, g-$C_3N_4$ and their heterojunction.

is the first-order apparent rate constant. The photocatalytic reduction rate constants are experimentally determined to be $0.001 \pm 0.0002\,h^{-1}$ for $Sr_{0.25}H_{1.5}Ta_2O_6\cdot H_2O$, $0.32 \pm 0.02\,h^{-1}$ for g-C_3N_4 and $0.57 \pm 0.07\,h^{-1}$ for $Sr_{0.25}H_{1.5}Ta_2O_6\cdot H_2O/50\,wt\%$–g-$C_3N_4$ heterojunction, respectively. Comparatively, the methyl orange degradation rate constants were determined to be $0.04 \pm 0.004\,h^{-1}$ for $Sr_{0.25}H_{1.5}Ta_2O_6\cdot H_2O$, $0.003 \pm 0.004\,h^{-1}$ for g-C_3N_4 and $0.27 \pm 0.02\,h^{-1}$ for $Sr_{0.25}H_{1.5}Ta_2O_6\cdot H_2O/50\,wt\%$–g-$C_3N_4$ heterojunction, respectively. Clearly, it is concluded that the heterojunction of $Sr_{0.25}H_{1.5}Ta_2O_6\cdot H_2O$ on g-C_3N_4 surfaces led to remarkable enhanced photocatalytic activity toward Cr(VI) photoreduction and methyl orange degradation in comparison to their individual counterpart.

The general principle for the enhanced photocatalytic performance of heterojunction photocatalysts is that they have different electronic energy levels so that charge separation can be enhanced. In order to get further insight into the energy levels of the conduction and valence band for $Sr_{0.25}H_{1.5}Ta_2O_6\cdot H_2O$ and g-C_3N_4 were determined. The conduction band edge potential of a semiconductor at the point of zero charge can be obtained by using Mulliken electronegativity theory, which is expressed as follow

$$E_{CB} = X - E^e - 0.5E_g$$

where E_{CB} is the conduction band edge potential, X is the absolute electronegativity of the semiconductor, which is the geometric mean of the electronegativity of the constituent atoms. The Mulliken electronegativity of the constituent atoms presents the arithmetic mean of the atomic electron affinity and the first ionization energy. E^e is the energy of free electrons in the hydrogen scale, which is about 4.5 eV [52]. E_g is the band gap energy of the semiconductor. The X value was calculated to be 6.44 eV for $Sr_{0.25}H_{1.5}Ta_2O_6\cdot H_2O$ and 4.72 eV for g-C_3N_4, respectively. Accordingly, the rough conduction band edge potential of $Sr_{0.25}H_{1.5}Ta_2O_6\cdot H_2O$ was determined to be −0.49 eV, and the valence band edge potential of $Sr_{0.25}H_{1.5}Ta_2O_6\cdot H_2O$ was estimated to be 4.29 eV. Meanwhile, the conduction band edge potential of g-C_3N_4 was calculated to be −1.09 eV, and the valence band edge potential of g-C_3N_4 was determined to be 1.53 eV, which is close to previous reported values [17]. Apparently, the conduction band edge potential of g-C_3N_4 is more negative than that of $Sr_{0.25}H_{1.5}Ta_2O_6\cdot H_2O$. Therefore, it is supposed that, under visible light irradiation, g-C_3N_4 in the heterojunction photocatalyst acts as a sensitizer to absorb photons as well as generates electron–hole pairs. Subsequently, the photogenerated electrons on g-C_3N_4 can easily transfer to the conduction band of $Sr_{0.25}H_{1.5}Ta_2O_6\cdot H_2O$ via the well developed interface,
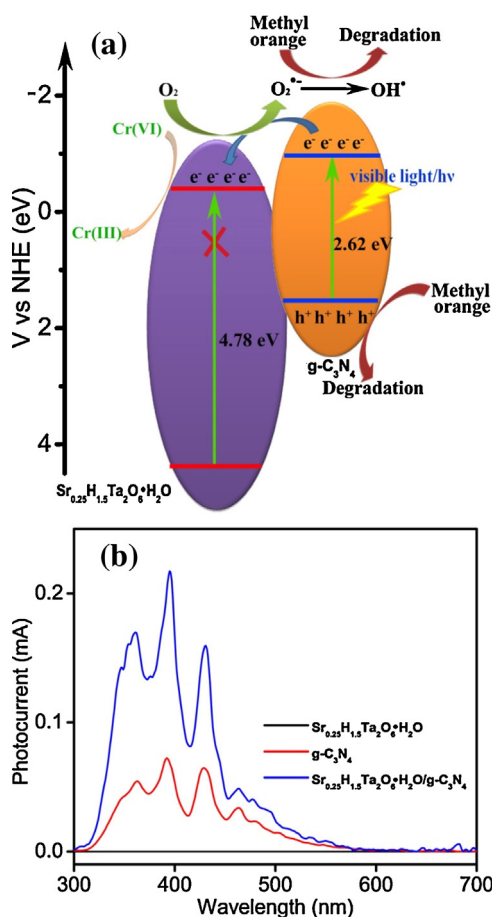
Fig. 7. Schematic diagram of electron–hole pairs' separation between $Sr_{0.25}H_{1.5}Ta_2O_6·H_2O$ and $g-C_3N_4$ (a), surface photocurrent of pristine $Sr_{0.25}H_{1.5}Ta_2O_6·H_2O$, $g-C_3N_4$ and $Sr_{0.25}H_{1.5}Ta_2O_6·H_2O/50$ wt%–$g-C_3N_4$ (b).
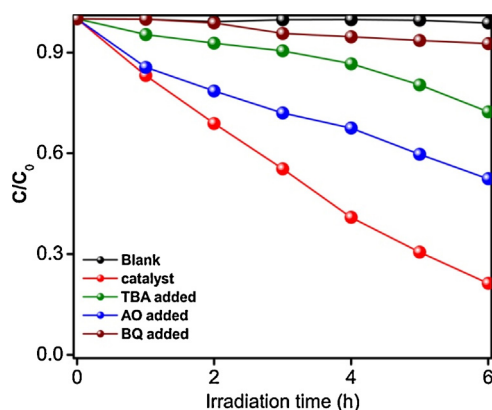
Fig. 8. Effects of different scavengers on methyl orange degradation in the presence of $Sr_{0.25}H_{1.5}Ta_2O_6·H_2O/50$ wt%–$g-C_3N_4$ under visible light irradiation.

leaving the holes on the valence band of $g-C_3N_4$, which is illustrated in Fig. 7a. This interfacial electron transfer process can undoubtedly lead to the suppression of electron–hole recombination process, thus enhancing the photocatalytic activity, which is further confirmed by the surface photocurrent spectra (Fig. 7b). As shown in Fig. 7b, the $Sr_{0.25}H_{1.5}Ta_2O_6·H_2O/g-C_3N_4$ heterojunction photocatalyst exhibited highest photocurrent intensity in comparison with pristine $Sr_{0.25}H_{1.5}Ta_2O_6·H_2O$ and $g-C_3N_4$, which strongly suggests that heterojunction of $Sr_{0.25}H_{1.5}Ta_2O_6·H_2O$ on $g-C_3N_4$ can enhance the charge separation efficiency and pro-

mote the photocatalytic performance. As mentioned above, the photogenrated electrons migrated to the conduction band of $Sr_{0.25}H_{1.5}Ta_2O_6·H_2O$, which energy potential is more negative than the reduction potential of $Cr_2O_7^{2-}/Cr^{3+}$ (1.27 V versus NHE), indicating the $Sr_{0.25}H_{1.5}Ta_2O_6·H_2O/g-C_3N_4$ heterojunction photocatalyst have powerful potential to reduce Cr(VI) to Cr(III) under visible light irradiation. Moreover, the conduction band edge potential is also more negative than that of $O_2/O_2^{•-}$ (−0.33 V versus NHE) [40]. This result suggests that generation of active oxygen species is possible for adsorption oxygen by capturing an electron from the conduction band of $Sr_{0.25}H_{1.5}Ta_2O_6·H_2O$, which may lead to the degradation of methyl orange. On the other hand, the photogenerated holes left in the valence band of $g-C_3N_4$, which energy potential is more negative than those of the standard redox potential for $OH^•/OH^-$ (1.9 V versus NHE) and $OH^•/H_2O$ (2.73 V versus NHE) [39], predicting the absence of $OH^•$ radical species in the photocatalytic process.

To further verify the primary photocatalytic radical species during the photocatalytic process over $Sr_{0.25}H_{1.5}Ta_2O_6·H_2O/g-C_3N_4$ heterojunction photocatalysts, controlled experiments were conducted by adding certain types of active species scavengers using methyl orange degradation as the model reaction [53]. Briefly, the photodegradation of methyl orange was repeated with modification by adding 1 mmol of benzoquinone (BQ) as a superoxide radical scavenger ($O_2^{•-}$), 10 mmol of ammonium oxalate (AO) as a hole (h^+) scavenger, and 10 mmol of *tert*-butyl alcohol (TBA) as a hydroxyl radical scavenger ($OH^•$). Under visible light irradiation, the photodegradation of methyl orange was apparently inhibited when BQ and AO were added, as shown in Fig. 8. This observation gives evidence that $O_2^{•-}$ active species and direct hole oxidation were involved in the photodegradation process of methyl orange. Surprisingly, the photodegradation rate of methyl orange was also decreased by adding TBA scavenger, suggesting $OH^•$ active species were generated and taken part in the photodegradation process. This result seems to be contrary to the above predictions, since the photogenerated holes in the valence band of $g-C_3N_4$ cannot oxidize OH^- or H_2O to produce $OH^•$ active species. A possible explanation is that the photogenrated $O_2^{•-}$ active species can react with electrons in succession to produce $OH^•$ active species [54].

Although the heterojunction of $Sr_{0.25}H_{1.5}Ta_2O_6·H_2O$ on $g-C_3N_4$ led to enhanced photocatalytic activity, the improvement of visible light absorption efficiency and photocatalytic performance for $Sr_{0.25}H_{1.5}Ta_2O_6·H_2O/g-C_3N_4$ is still urgent and necessary. Due to the surface plasmonic properties, silver decorated on semiconductors can enhance the harvesting of visible light and the subsequent photocatalytic performance [55]. In this work, Ag nanoparticles decorated $Sr_{0.25}H_{1.5}Ta_2O_6·H_2O/g-C_3N_4$ heterojunction photocatalysts were prepared via a photoreduction method using methyl orange as hole scavenger. Since the photogenerated electrons were migrated from $g-C_3N_4$ valence band to the valence band of $Sr_{0.25}H_{1.5}Ta_2O_6·H_2O$, Ag nanoparticles can deposit on $Sr_{0.25}H_{1.5}Ta_2O_6·H_2O$ surfaces as confirmed by TEM observations. Moreover, it is inevitable that partial Ag nanoparticles may also deposit on the interfaces between $Sr_{0.25}H_{1.5}Ta_2O_6·H_2O$ and $g-C_3N_4$ (Fig. S10), being beneficial for the formation of Ohmic contact that could accelerate the charge transfer rate [56] between $Sr_{0.25}H_{1.5}Ta_2O_6·H_2O$ and $g-C_3N_4$ and enormously enhance the photocatalytic activity. Generally, the content of noble metal nanoparticles loading on semiconductors is often varied with the initial ones. Fig. S11 illustrates the as-measured Ag loading content as a function of initial ones. The final weight contents of Ag in the ternary heterojunctions were all smaller than the initial ones. Increasing the initial Ag content causes the Ag content in the final samples to increase, which varies from 0.38 wt% to 2.11%. Fig. 9a shows the photoreduction spectra of Cr(VI) over Ag decorated $Sr_{0.25}H_{1.5}Ta_2O_6·H_2O/g-C_3N_4$ as
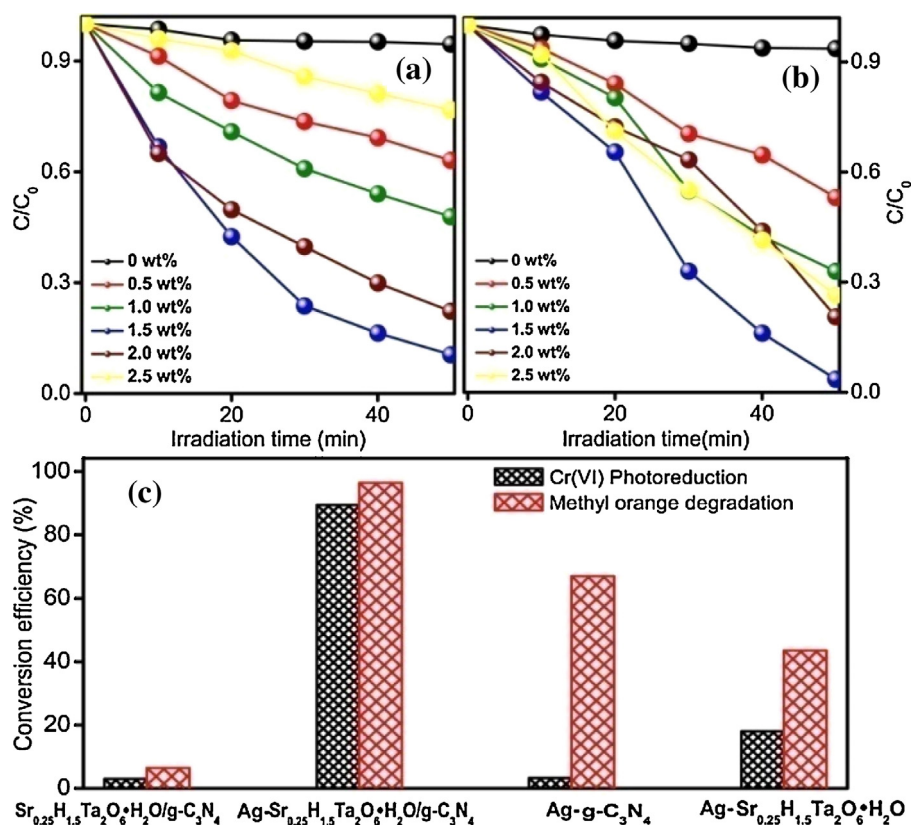
Fig. 9. Normalized concentration of Cr(VI) versus visible light irradiation time in the presence of Ag decorated $Sr_{0.25}H_{1.5}Ta_2O_6 \cdot H_2O/g\text{-}C_3N_4$ heterojunction photocatalysts (a), methyl orange concentration changes as a function of visible light irradiation time (b), Cr(VI) and methyl orange conversion efficiencies in initial 50 min over Ag modified photocatalysts.

a function of Ag loading content. Under visible light irradiation, all Ag decorated $Sr_{0.25}H_{1.5}Ta_2O_6 \cdot H_2O/g\text{-}C_3N_4$ photocatalysts demonstrated the capability for the photoreduction of Cr(VI), which showed a optimal performance at 1.5 wt% Ag decorated $Sr_{0.25}H_{1.5}Ta_2O_6 \cdot H_2O/g\text{-}C_3N_4$. The apparent rate constant (k) for 1.5 wt% Ag decorated $Sr_{0.25}H_{1.5}Ta_2O_6 \cdot H_2O/g\text{-}C_3N_4$ was determined by linear estimation using pseudo first order reaction kinetic, which was calculated to be $0.045 \pm 0.001 \, min^{-1}$ (Fig. S12). It is clearly that the optimal photoreduction performance achieved more than 4.7-fold in comparison to the value for $Sr_{0.25}H_{1.5}Ta_2O_6 \cdot H_2O/50 \, wt\%\text{-}g\text{-}C_3N_4$ heterojunction photocatalyst. Moreover, the optimal apparent quantum efficiency was also calculated to be 0.206% for Cr(VI) photoreduction (S13), which is much higher than that of 0.032% for $Sr_{0.25}H_{1.5}Ta_2O_6 \cdot H_2O/50 \, wt\%\text{-}g\text{-}C_3N_4$ heterojunction photocatalyst. Further increase of Ag loading content led to an apparent decrease of photocatalytic activity, which is basically related to the surface plasmon resonance photoabsorption intensity (Fig. S14) [57]. As for the photodegradation of methyl orange (Fig. 9b), Ag decorated $Sr_{0.25}H_{1.5}Ta_2O_6 \cdot H_2O/g\text{-}C_3N_4$ photocatalysts exhibited similar photocatalytic behavior with the photoreduction of Cr(VI) process, which showed the maximized photocatalytic activity at Ag loading content of 1.5 wt%. The apparent rate constant for methyl orange degradation over Ag decorated $Sr_{0.25}H_{1.5}Ta_2O_6 \cdot H_2O/50 \, wt\%\text{-}g\text{-}C_3N_4$ heterojunction photocatalyst was determined to be $0.064 \pm 0.01 \, min^{-1}$ (Fig. S15), which is 14.2 times higher than that of $Sr_{0.25}H_{1.5}Ta_2O_6 \cdot H_2O/50 \, wt\%\text{-}g\text{-}C_3N_4$. HPLC chromatograms of methyl orange and after photocatalytic degradation for different irradiation time confirmed the degradation process of methyl orange in the presence of Ag–$Sr_{0.25}H_{1.5}Ta_2O_6 \cdot H_2O/50 \, wt\%\text{-}g\text{-}C_3N_4$ heterojunction (Fig. S16) [58]. From Fig. S16, the prominent peak of the methyl orange

at 2.45 min was observed to diminish gradually with continuous photocatalytic reaction. Moreover, TOC data was also given to investigate the mineralization of methyl orange (Fig. S17) [59]. From TOC data, it is clearly seen that the TOC value gradually decreased with prolonging the visible light irradiation time but was not completely mineralized in initial 50 min, suggesting the mineralization of methyl orange can be achieved by Ag–$Sr_{0.25}H_{1.5}Ta_2O_6 \cdot H_2O/50 \, wt\%\text{-}g\text{-}C_3N_4$ heterojunctions. According to previous literature [60,61], the optimal apparent quantum efficiency was also determined to be $1.860 \times 10^{-7} \, mmol \, min^{-1} \, mW^{-1}$ toward methyl orange photodegradation (S13). As well-documented in previous literatures [62–65], the degradation of dyes often occurs via direct (band gap excitation mechanism) and/or indirect effects (dye sensitized mechanism). It is therefore necessary to specify the degradation mechanism, which is helpful to reveal the catalytic activity of the as-prepared photocatalysts. Fig. S18 gives the time dependent absorption spectrum of methyl orange aqueous solutions during the visible light irradiation in the presence of 1.5 wt%-Ag–$Sr_{0.25}H_{1.5}Ta_2O_6 \cdot H_2O/50 \, wt\%\text{-}g\text{-}C_3N_4$ sample. During the irradiation, no apparent absorptions were observed, while the hypsochromic shift was extremely small, which indicates the methyl orange degradation is likely to be mainly governed by band gap excitation mechanism. Similar observation was reported by Qiu and coworkers in Co^{2+} doped ZnO for rhodamine B degradation under ultraviolet and visible light irradiation [66]. To further investigate the photocatalytic performance of the as-prepared photocatalysts, the photodegradation of phenol was investigated. From Fig. S19, it is seen that the C/C_0 value gradually decreased with prolonging the visible light irradiation time, suggesting the degra-
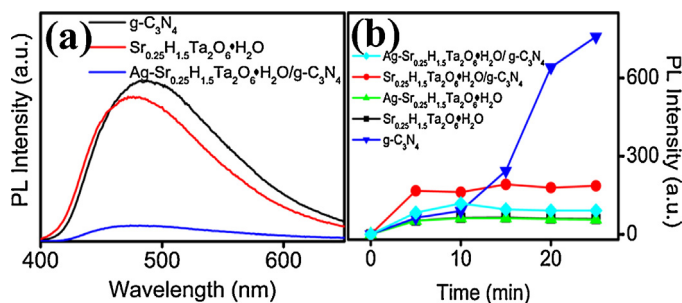
Fig. 10. Photoluminescence spectra of pristine g-C_3N_4, $Sr_{0.25}H_{1.5}Ta_2O_6 \cdot H_2O$/50 wt%–g-$C_3N_4$ and 1.5 wt% Ag–$Sr_{0.25}H_{1.5}Ta_2O_6 \cdot H_2O$/50 wt%–g-$C_3N_4$ (a). The generation of OH$^\bullet$ during the photocatalysis over the as-prepared samples under visible light irradiation (b).

Fig. 11. EPR spectra obtained from 1.5 wt% Ag–$Sr_{0.25}H_{1.5}Ta_2O_6 \cdot H_2O$/50 wt%–g-$C_3N_4$ sample containing 0.22 M DMPO and 4.0 mg catalyst with total volume of 2 mL water (a) and 90% methanol/10% water (b) under different visible light irradiation time.

dation of phenol over the as-prepared photocatalysts can also be achieved.

To further shed light on the surface plasmon resonance effects on the enhanced photocatalytic activity, Ag nanoparticles were decorated on pristine $Sr_{0.25}H_{1.5}Ta_2O_6 \cdot H_2O$ and g-C_3N_4 for comparison. As shown in Fig. 9c, the conversion efficiencies of 1.5 wt%-Ag–$Sr_{0.25}H_{1.5}Ta_2O_6 \cdot H_2O$/50 wt%–g-$C_3N_4$ toward Cr(VI) photoreduction and methyl orange degradation were achieved to be 89.5% and 96.5%, respectively, which is much larger than that of $Sr_{0.25}H_{1.5}Ta_2O_6 \cdot H_2O$/50 wt%–g-$C_3N_4$. As discussed above, the bandgap energy was determined to be 4.78 eV, demonstrating no apparent photocatalytic activity toward Cr(VI) photoreduction and methyl orange degradation under visible light irradiation. However, it is noted that Ag nanoparticles loaded on $Sr_{0.25}H_{1.5}Ta_2O_6 \cdot H_2O$ showed apparent visible light photocatalytic activity toward Cr(VI) photoreduction and methyl orange degradation with conversion efficiencies of 18% and 43%, respectively. Therefore, it is suggested that the surface plasmon resonance of Ag on $Sr_{0.25}H_{1.5}Ta_2O_6 \cdot H_2O$ nanoparticles enhanced the visible light absorption efficiency (Fig S14) and subsequently improved the photocatalytic performance. Moreover, Ag decorated g-C_3N_4 photocatalyst was also prepared for comparison. As indicated in Fig. 9c, Ag loaded on g-C_3N_4 also exhibited enhanced photocatalytic activity in comparison with pristine g-C_3N_4, which showed conversion efficiencies of 3.3% and 67% toward Cr(VI) photoreduction and methyl orange degradation, respectively. The enhancement of the photocatalytic activity for g-C_3N_4 via Ag loading has been well documented by previous literatures [67]. Ag nanoparticles prefer to act as electron traps to facilitate the separation of photogenerated charge carriers and accelerate the interfacial charge transfer process [68]. To further specify the key roles of Ag nanoparticles on the highly enhanced photocatalytic activity and the underlying photocatalytic mechanism, the photoluminescence spectra and primary active species analyses were also carried. Photoluminescence spectra has been widely applied to reveal the migration of photogenerated charge carriers in the semiconductor heterojunctions [69,70]. From Fig. 10a, it is seen that all as-prepared samples exhibited similar emission band in the range of 400–700 nm. Interestingly, the photoluminescence intensity of $Sr_{0.25}H_{1.5}Ta_2O_6 \cdot H_2O$/50 wt%–g-$C_3N_4$ heterojunction is lower than that of pristine g-C_3N_4. Furthermore, the photoluminescence intensity of 1.5 wt% Ag–$Sr_{0.25}H_{1.5}Ta_2O_6 \cdot H_2O$/50 wt% g-$C_3N_4$ heterojunction was greatly weakened. Based on the photoluminescence analysis, it is evident that the recombination of charge carriers is extremely suppressed in $Sr_{0.25}H_{1.5}Ta_2O_6 \cdot H_2O$/50 wt%–g-$C_3N_4$ and 1.5 wt% Ag–$Sr_{0.25}H_{1.5}Ta_2O_6 \cdot H_2O$/50 wt%–g-$C_3N_4$ heterojunction, mainly owing to the formation of heterojunction structures by which the efficient separation of charge carriers is achieved. This observation gave an evidence that, under visible light irradiation, the photogenerated electrons in the conduction band of g-C_3N_4

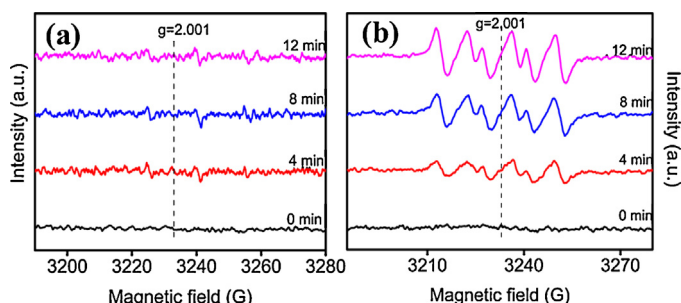prefer to migrate to the conduction band of $Sr_{0.25}H_{1.5}Ta_2O_6 \cdot H_2O$, which results in the separation of photogenerated charge carriers, leading to that Ag nanoparticles are likely to deposit on the surface of $Sr_{0.25}H_{1.5}Ta_2O_6 \cdot H_2O$ and the interface between $Sr_{0.25}H_{1.5}Ta_2O_6 \cdot H_2O$ and g-C_3N_4. To further elucidate the photodegradation mechanism of the as-prepared samples, the reactive oxidative species were tested. It is generally accepted that OH$^\bullet$ and $O_2^{\bullet-}$ active species are the main reactive oxidative species in photocatalytic degradation reactions [71]. t-BuOH is a well-known OH$^\bullet$ scavenger, which can react quickly with OH$^\bullet$ with a rate constant of 6.0×10^8 M^{-1} s^{-1} [72]. As exhibited in Fig. 10b, the as-prepared samples showed different abilities for generating OH$^\bullet$ active species. It is seen that $Sr_{0.25}H_{1.5}Ta_2O_6 \cdot H_2O$ and Ag–$Sr_{0.25}H_{1.5}Ta_2O_6 \cdot H_2O$ showed no apparent ability for generating OH$^\bullet$ active species, while pristine g-C_3N_4 exhibited highest ability for generating OH$^\bullet$ active species. The $Sr_{0.25}H_{1.5}Ta_2O_6 \cdot H_2O$/g-$C_3N_4$ heterojunction gave moderate ability for generating OH$^\bullet$ active species, suggesting OH$^\bullet$ active species take part in the photodegradation process as confirmed by the trapping experiment (Fig. 8). However, the generating ability of OH$^\bullet$ active species was highly suppressed for $Sr_{0.25}H_{1.5}Ta_2O_6 \cdot H_2O$/g-$C_3N_4$ heterojunction after Ag loading. This result can be verified by electron paramagnetic resonance (EPR) spectra [73]. The formation of OH$^\bullet$ and $O_2^{\bullet-}$ active species was examined by the EPR technique. 5,5-Dimethyl-1-pyrroline-N-oxide (DMPO) was used as a spin trap to capture hydroxyl radical and superoxide species [74]. For 1.5 wt% Ag–$Sr_{0.25}H_{1.5}Ta_2O_6 \cdot H_2O$/50 wt%–g-$C_3N_4$ heterojunction without visible light irradiation, no characteristic EPR signal was detected. Upon irradiation for 12 min, very weak characteristic EPR peaks belonging to DMPO–$^\bullet$OH adduct was observed (Fig. 11a), indicating that OH$^\bullet$ is not the major active species during the photocatalytic process. From Fig. 11b, it can be seen that no DMPO–$O_2^{\bullet-}$ adduct (in methanol solution) are observed, but after 4 min of visible light irradiation, the characteristic sextet peaks of DMPO–$O_2^{\bullet-}$ spin adduct was observed. Moreover, the intensity of DMPO–$O_2^{\bullet-}$ signals increased with prolonged irradiation time. This observation predicts that $O_2^{\bullet-}$ active species may play important role in the photocatalytic degradation of methyl orange. EPR technique confirms the formation of OH$^\bullet$ and $O_2^{\bullet-}$ active species during the photocatalytic process and gives direct evidence that OH$^\bullet$ and $O_2^{\bullet-}$ active species are responsible for the photodegradation of methyl orange.

For potential applications, the stability of the heterojunction photocatalyst should be taken into consideration. Fig. 12 a shows the XRD patterns of Ag decorated $Sr_{0.25}H_{1.5}Ta_2O_6 \cdot H_2O$/g-$C_3N_4$ heterojunction photocatalyst before and after catalytic reaction. No structural difference between the samples before and after reaction is observable, confirming the high structural stability of Ag decorated $Sr_{0.25}H_{1.5}Ta_2O_6 \cdot H_2O$/g-$C_3N_4$ heterojunction photocatalyst. Meanwhile, no obvious changes of Ag 3d XPS spectra was observed

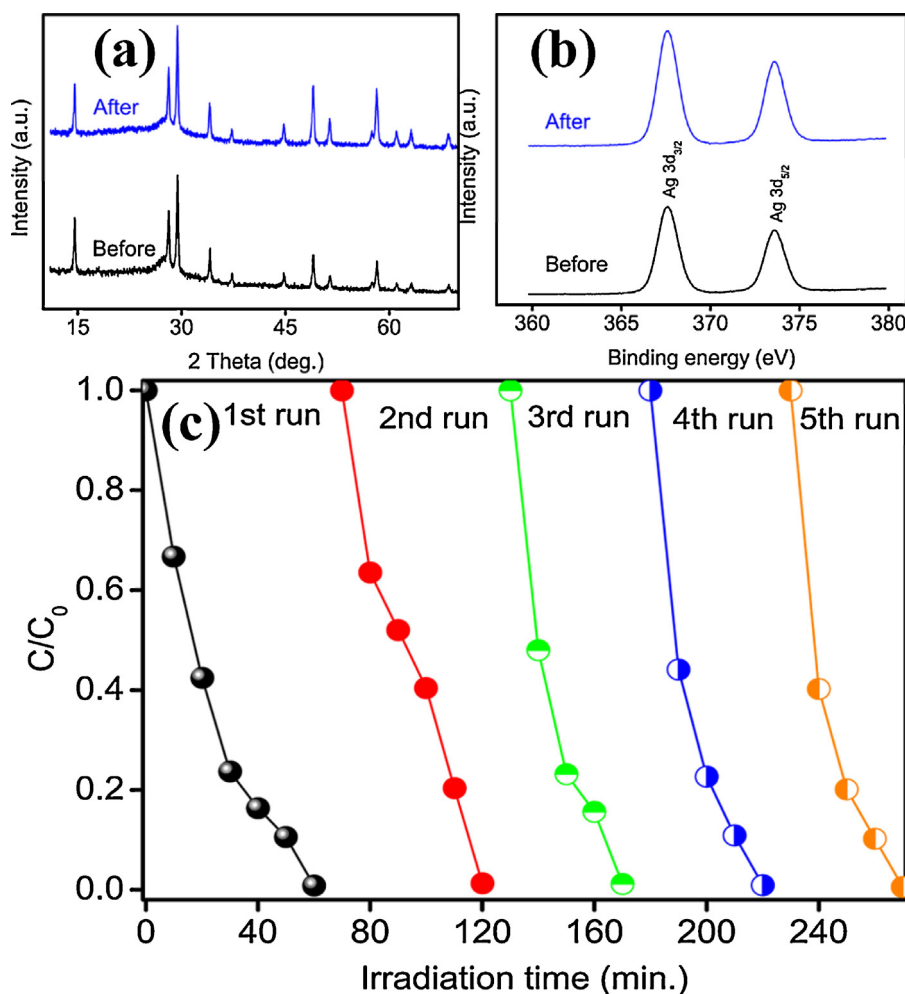**Fig. 12.** XRD patterns (a) and Ag 3d XPS spectra (b) of Ag decorated $Sr_{0.25}H_{1.5}Ta_2O_6 \cdot H_2O$/g-$C_3N_4$ heterojunction photocatalysts before and after photocatalytic reaction. Cyclic degradation curve for the 1.5 wt% Ag decorated $Sr_{0.25}H_{1.5}Ta_2O_6 \cdot H_2O$/g-$C_3N_4$.

for the heterojunction photocatalyst before and after the catalytic reaction (Fig. 12b). And very small amount of the as-measured Ag content changed before and after the reaction, which varied from 1.28 wt% to 1.19 wt%. The cyclic stability of the heterojunction photocatalyst was evaluated by repeating experiments on the degradation of methyl orange under visible light irradiation using 1.5 wt% Ag decorated $Sr_{0.25}H_{1.5}Ta_2O_6 \cdot H_2O$/g-$C_3N_4$. After each run, the catalysts were collected and washed by simple filtration followed by ultrasonic cleaning with deionized water. As shown in Fig. 12c, the photocatalytic efficiency showed no apparent loss even after five successive cycles, indicating that the heterojunction photocatalysts were highly stable and were not photocorroded during the photocatalytic degradation of methyl orange under visible light irradiation.

Having these results in mind, a more plausible explanation for the enhanced photocatalytic activity of Ag decorated $Sr_{0.25}H_{1.5}Ta_2O_6 \cdot H_2O$/g-$C_3N_4$ heterojunction photocatalysts can be described in Fig. 13. Under visible light irradiation, the incident photons could be absorbed by Ag nanoparticles, which was separated into electrons and holes in terms of the surface plasmoinc resonance induced local electromagnetic field [75]. The photogenerated electrons are injected from the Ag nanoparticles into the conduction band of $Sr_{0.25}H_{1.5}Ta_2O_6 \cdot H_2O$, leaving the resultant electron-deficient Ag nanoparticles that oxidize methyl orange for degradation and return to their original metallic state. On the other hand, partial Ag nanoparticles deposited at the interfacial
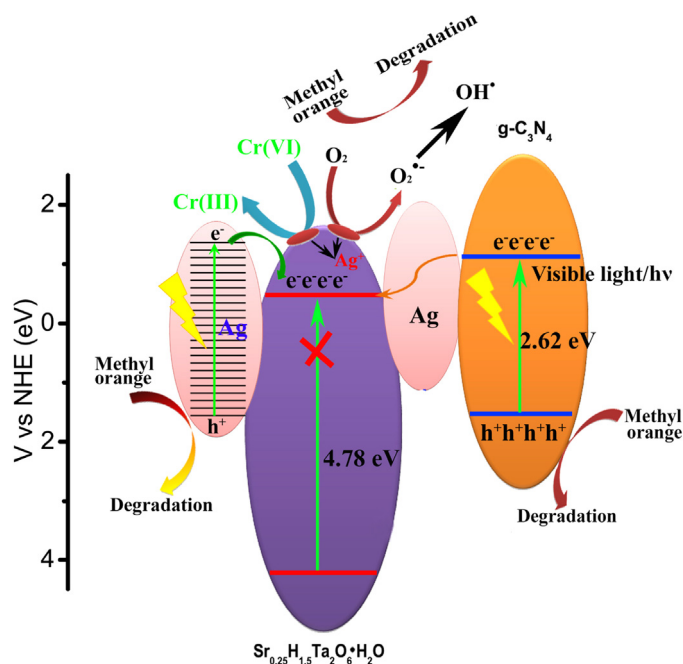

Fig. 13. Illustration of possible mechanism for Cr(VI) photoreduction and methyl orange degradation over Ag decorated $Sr_{0.25}H_{1.5}Ta_2O_6 \cdot H_2O$/-g-$C_3N_4$ photocatalytic system under visible light irradiation.

site may establish an Ohmic contact between $Sr_{0.25}H_{1.5}Ta_2O_6 \cdot H_2O$ and g-C_3N_4. The photogenerated electrons from the conduction band of g-C_3N_4 can readily transfer to the conduction band of $Sr_{0.25}H_{1.5}Ta_2O_6 \cdot H_2O$ using Ag as a electron mediator, which would greatly enhance the electron–hole pair separation efficiency. In this photocatalytic reaction system, the photogenerated electrons in the conduction band of $Sr_{0.25}H_{1.5}Ta_2O_6 \cdot H_2O$ could react with electron acceptors such as $Cr_2O_7^{2-}$ or O_2 existed in the system, leading to the photoreduction of Cr(VI) or the formation of $O_2^{\bullet-}$ active species. The holes in the valence band of g-C_3N_4 and the photogenerated $O_2^{\bullet-}$ active species are responsible for the degradation of methyl orange.

4. Conclusion

A novel ternary component Ag–$Sr_{0.25}H_{1.5}Ta_2O_6 \cdot H_2O$/g-$C_3N_4$ photocatalytic system was constructed with highly enhanced visible light photocatalytic properties toward environmental remediation. The heterojunction of $Sr_{0.25}H_{1.5}Ta_2O_6 \cdot H_2O$ on g-C_3N_4 surfaces led to enhanced photocatalytic activity of $Sr_{0.25}H_{1.5}Ta_2O_6 \cdot H_2O$/g-$C_3N_4$ toward Cr(VI) photoreduction and methyl orange degradation in comparison with the pristine $Sr_{0.25}H_{1.5}Ta_2O_6 \cdot H_2O$ and g-C_3N_4 under visible light irradiation. The matching of the band structure between $Sr_{0.25}H_{1.5}Ta_2O_6 \cdot H_2O$ and g-C_3N_4 induced an efficient photogenerated electron transfer from the conduction band of g-C_3N_4 to the conduction band of $Sr_{0.25}H_{1.5}Ta_2O_6 \cdot H_2O$, resulting in efficient separation of the photogenerated electron–hole pairs and the subsequent promotion of photocatalytic activity. Moreover, Ag nanoparticles decorated on $Sr_{0.25}H_{1.5}Ta_2O_6 \cdot H_2O$/g-$C_3N_4$ can enhance the visible light absorption efficiency and robustly improve the photocatalytic activity by a factor of 4.7 for Cr(VI) photoreduction and 14.2 for methyl orange degradation, respectively. The decoration Ag nanoparticles on $Sr_{0.25}H_{1.5}Ta_2O_6 \cdot H_2O$/g-$C_3N_4$ not only extended the visible light absorption region due to surface plasmon resonance effects, but also acted as an electron mediator and electron acceptor for efficient charge separation and enhancement of photocatalytic activity. This study provides hints for the fabrication of novel and highly efficient ternary photocatalysts and facilitates their practical applications for environmental remediation.

Acknowledgements

Appendix A. Supplementary data

Supplementary data associated with this article can be found, in the online version, at http://dx.doi.org/10.1016/j.apcatb.2015.07.052

References

[1] X.B. Chen, L. Liu, P.Y. Yu, S.S. Mao, Science 221 (2011) 746–750.
[2] X. Yao, X. Liu, X. Hu, ChemCatChem 6 (2014) 3409–3418.
[3] A. Hameed, M. Aslam, I.M.I. Ismail, N. Salah, P. Fornasiero, Appl. Catal. B: Environ. 163 (2014) 444–451.
[4] Y. Luo, X. Liu, X. Tang, Y. Luo, Q. Zeng, X. Deng, S. Ding, Y. Sun, J. Mater. Chem. A 2 (2014) 14927–14939.
[5] T. Grewe, K. Meier, H. Tüysüz, Catal. Today 225 (2014) 142–148.
[6] J. Boltersdorf, T. Wong, P.A. Maggard, ACS Catal. 3 (2013) 2943–2953.
[7] C.W. Lee, H.K. Park, S. Park, H.S. Han, S.W. Seo, H.J. Song, S. Shin, D.W. Kim, K.S. Hong, J. Mater. Chem. A 3 (2015) 825–831.
[8] Y. Hu, Y. Cao, P. Wang, D. Li, W. Chen, Y. He, X. Fu, Y. Shao, Y. Zheng, Appl. Catal. B: Environ. 125 (2012) 294–303.
[9] A. Iwase, H. Kato, A. Kudo, Appl. Catal. B: Environ. 136–137 (2013) 89–93.
[10] M. Aslam, I.M.I. Ismail, S. Chandrasekaran, A. Hameed, J. Hazard. Mater. 276 (2014) 120–128.
[11] J. Yu, J. Low, W. Xiao, P. Zhou, M. Jaroniec, J. Am. Chem. Soc. 136 (2014) 8839–8842.
[12] C. Huang, Z. Long, M. Miyauchi, X. Qiu, CrystEngComm 16 (2014) 4967–4972.
[13] Y.J. Yao, J.C. Qin, H. Chen, F.X. Wei, X.T. Liu, J.L. Wang, S.B. Wang, J. Hazard. Mater. 291 (2015) 28–37.
[14] D.D. Qin, C.L. Tao, RSC Adv. 4 (2014) 16968–16972.
[15] X. Wang, S. Li, Y. Ma, H. Yu, J. Yu, J. Phys. Chem. C 115 (2011) 14648–14655.
[16] S. Liang, L. Shen, J. Zhu, Y. Zhang, X. Wang, Z. Li, L. Wu, X. Fu, RSC Adv. 1 (2011) 458–467.
[17] S. Cao, J. Yu, J. Phys. Chem. Lett. 5 (2014) 2101–2107.
[18] F. Su, S.C. Mathew, G. Lipner, X. Fu, M. Antonietti, S. Blechert, X. Wang, J. Am. Chem. Soc. 132 (2010) 16299–16301.
[19] Z.W. Zhao, Y.J. Sun, F. Dong, Nanoscale 7 (2014) 15–37.
[20] C.C. Han, L. Ge, C.F. Chen, Y.J. Li, X.L. Xiao, Y.N. Zhang, L.L. Guo, Appl. Catal. B: Environ. 147 (2014) 546–553.
[21] L. Ge, C.C. Han, X.L. Xiao, L.L. Guo, Appl. Catal. B: Environ. 142–143 (2013) 414–422.
[22] H. Shi, G. Chen, C. Zhang, Z. Zou, ACS Catal. 4 (2014) 3637–3643.
[23] H. Wang, L. Zhang, Z. Chen, J. Hu, S. Li, Z. Wang, J. Liu, X. Wang, Chem. Soc. Rev. 43 (2014) 5234–5244.
[24] J. Li, S.K. Cushing, P. Zheng, T. Senty, F. Meng, A.D. Bristow, A. Manivannan, N. Wu, J. Am. Chem. Soc. 136 (2014) 8438–8449.
[25] S. Linic, P. Christopher, D.B. Ingram, Nat. Mater. 10 (2011) 911–921.
[26] Z. Bian, T. Tachikawa, P. Zhang, M. Fujitsuka, T. Majima, J. Am. Chem. Soc. 136 (2014) 458–465.
[27] J. Li, S.K. Cushing, J. Bright, F. Meng, T.R. Senty, P. Zheng, A.D. Bristow, N. Wu, ACS Catal. 3 (2013) 47–51.
[28] Y. Wu, H. Liu, J. Zhang, F. Chen, J. Phys. Chem. C 113 (2009) 14689–14695.
[29] S.C. Yan, Z.S. Li, Z.G. Zou, Langmuir 25 (2009) 10397–10401.
[30] T. Jiang, T. Xie, L. Chen, Z. Fu, D. Wang, Nanoscale 5 (2013) 2938–2944.
[31] L.S. Clesceri, A.E. Greenberg, A.D. Eaton, Standard Methods for the Examination of Water and Wastewater, 20th ed., American Public Health Association, Washington, DC, 1998.
[32] X. Bai, L. Wang, R. Zong, Y. Zhu, J. Phys. Chem. C 117 (2013) 9952–9961.
[33] H.L. Li, Z.N. Du, G.L. Wang, Y.C. Zhang, Mater. Lett. 64 (2010) 431–434.
[34] J.Q. Wang, S.Y. Su, B. Liu, M.H. Cao, C.W. Hu, Chem. Commun. 49 (2013) 7830–7832.
[35] L.Q. Ye, J.Y. Liu, Z. Jiang, T.Y. Peng, L. Zan, Appl. Catal. B: Environ. 142–143 (2013) 1–7.
[36] G.G. Zhang, J.S. Zhang, M.W. Zhang, X.C. Wang, J. Mater. Chem. 22 (2012) 8083–8091.
[37] M.J. Muñoz-Batista, M.A. Nasalevich, T.J. Savenije, F. Kapteijn, J. Gascon, A. Kubacka, M. Fernández-García, Appl. Catal. B: Environ. 176–177 (2015) 687–698.
[38] B.Z. Tian, T.T. Wang, R.F. Dong, S.Y. Bao, F. Yang, J.L. Zhang, Appl. Catal. B: Environ. 147 (2014) 22–28.
[39] Y. Su, G. Li, X. Wang, L. Li, J. Lumin. 132 (2012) 1407–1413.
[40] Y. Su, L. Peng, J. Guo, S. Huang, L. Lv, X. Wang, J. Phys. Chem. C 118 (2014) 10728–10739.
[41] L. Sun, X. Zhao, C.J. Jia, Y. Zhou, X. Cheng, P. Li, L. Liu, W. Fan, J. Mater. Chem. 22 (2012) 23428–23438.
[42] Z. Zhang, J. Huang, M. Zhang, Q. Yuan, B. Dong, Appl. Catal. B: Environ. 163 (2015) 298–305.
[43] X. Yan, X. Wang, W. Gu, M. Wu, Y. Yan, B. Hu, G. Che, D. Han, J. Yang, W. Fan, W. Shi, Appl. Catal. B: Environ. 164 (2015) 297–304.
[44] D. Jiang, L. Chen, J. Xie, M. Chen, Dalton Trans. 43 (2014) 4878–4885.
[45] C. Xing, Z. Wu, D. Jiang, M. Chen, J. Colloid Interf. Sci. 433 (2014) 9–15.
[46] H. Lin, L. Li, M. Zhao, X. Huang, X. Chen, G. Li, R. Yu, J. Am. Chem. Soc. 134 (2012) 8328–8331.
[47] M. Sun, D. Li, W. Li, Y. Chen, Z. Chen, Y. He, X. Fu, J. Phys. Chem. C 112 (2008) 18076–18081.
[48] W. Li, D. Li, Y. Lin, P. Wang, W. Chen, X. Fu, Y. Shao, J. Phys. Chem. C 116 (2012) 3552–3560.
[49] Y.R. Smith, A. Kar, V. Subramanian, Ind. Eng. Chem. Res. 48 (2009) 10268–10276.
[50] A. Neren Ökte, Ö. Yilmaz, Appl. Catal. B: Environ. 85 (2008) 92–102.
[51] X.H. Wang, J.G. Li, H. Kamiyama, Y. Moriyoshi, T. Ishigaki, J. Phys. Chem. B 110 (2006) 6804–6809.
[52] Y. Su, X. Xin, Y. Wang, T. Wang, X. Wang, Chem. Commun. 50 (2014) 4200–4202.
[53] L.L. Chen, D.L. Jiang, T. He, Z.D. Wu, M. Chen, CrystEngComm 15 (2013) 7556–7563.
[54] W. Liu, M. Wang, C. Xu, S. Chen, Chem. Eng. J. 209 (2012) 386–393.
[55] D. Chen, T. Li, Q. Chen, J. Gao, B. Fan, J. Li, X. Li, R. Zhang, J. Sun, L. Gao, Nanoscale 4 (2012) 5431–5439.
[56] P. Zhou, J. Yu, M. Jaroniec, Adv. Mater. 26 (2014) 4920–4935.
[57] D. Jiang, W. Wang, S. Sun, L. Zhang, Y. Zheng, ACS Catal. 5 (2015) 613–621.
[58] M. Zhang, J. Xu, R. Zong, Y. Zhu, Appl. Catal. B: Environ. 147 (2014) 229–235.
[59] H. Yang, T. An, G. Li, W. Song, W.J. Cooper, H. Luo, X. Guo, J. Hazard. Mater. 179 (2010) 834–939.
[60] N. Serpone, A. Salinaro, Pure Appl. Chem. 71 (1999) 303–320.
[61] M.R. Hoffmann, S.T. Martin, W. Choi, D.W. Bahnemann, Chem. Rev. 95 (1995) 69–96.

[62] K. Vinodgopal, D.E. Wynkoop, P.V. Kamat, Environ. Sci. Technol. 30 (1996) 1660–1666.
[63] C. Nasr, K. Vinodgopal, L. Fisher, S. Hotchandani, A.K. Chattopadhyay, P.V. Kamat, J. Phys. Chem. 100 (1996) 8436–8442.
[64] Y. Park, Y. Na, D. Pradhan, B.K. Min, Y. Sohn, CrystEngComm 16 (2014) 3155–3167.
[65] X. Yan, T. Ohno, K. Nishijima, R. Abe, B. Ohtani, Chem. Phys. Lett. 429 (2006) 606–610.
[66] X. Qiu, G. Li, X. Sun, L. Li, X. Fu, Nanotechnology 19 (2008) 215703–215708.
[67] X. Lü, J. Shen, Z. Wu, J. Wang, J. Xie, J. Mater. Res. 29 (2014) 2170–2178.
[68] L. Ge, C. Huan, J. Liu, Y. Li, Appl. Catal. A: Gen. 409–410 (2011) 215–222.
[69] F. Chang, Y. Xie, J. Zhang, J. Chen, C. Li, J. Wang, J. Luo, B. Deng, X. Hu, RSC Adv. 4 (2014) 28519–29528.
[70] P. Niu, L. Zhang, G. Liu, H.M. Cheng, Adv. Funct. Mater. 22 (2012) 4763–4770.
[71] H. Lin, L. Ding, Z. Pei, Y. Zhou, J. Long, W. Deng, X. Wang, Appl. Catal. B: Environ. 160–161 (2014) 98–105.
[72] Z. He, Y. Shi, C. Gao, L. Wen, J. Chen, S. Song, J. Phys. Chem. C 118 (2014) 389–398.
[73] J. Jiang, L. Zhang, H. Li, W. He, J.J. Yin, Nanoscale 5 (2013) 10573–10581.
[74] M. Li, X. Li, G. Jiang, G. He, Ceram. Int. 41 (2015) 5749–5757.
[75] R. Dong, B. Tian, C. Zeng, T. Li, T. Wang, J. Zhang, J. Phys. Chem. C 117 (2013) 213–220.